PAPER

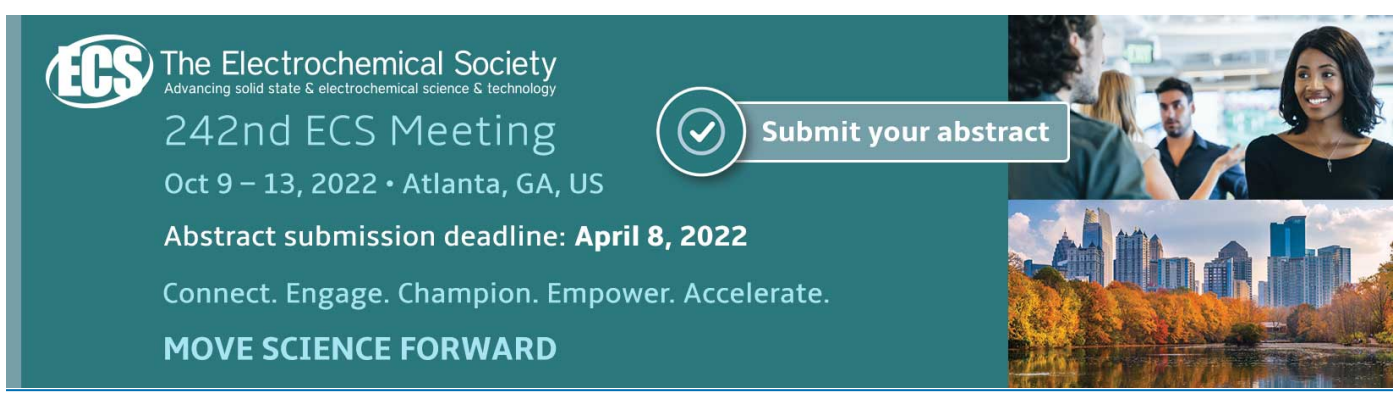
MAPbBr₃ nanocrystals from aqueous solution for poly(methyl methacrylate)-MAPbBr₃ nanocrystal films with compression-resistant photoluminescence

To cite this article: Xiaobing Tang et al 2022 Nanotechnology 33 235605

View the article online for updates and enhancements.

You may also like

- A Layered Photo-Anode Prepared Using TiO₂ Nanocrystals with Different Sizes for Enhanced Light-Trapping in Quantum Dots-Sensitized Solar Cells Jianping Deng, Minqiang Wang, Junfei Fang et al.
- Study of classical thermo-mechanical equations in ultrafast thermo-elastic domain: electronic sputtering from metal-dielectric nanocomposites Fouran Singh, J P Stoquert and J C Pivin
- (Invited) Facile Manufacturing of Colloidal <u>Nanocrystals to Macroscale Film</u> Don-Hyung Ha



IOP Publishing Nanotechnology

Nanotechnology 33 (2022) 235605 (14pp)

https://doi.org/10.1088/1361-6528/ac59e8

MAPbBr₃ nanocrystals from aqueous solution for poly(methyl methacrylate)-MAPbBr₃ nanocrystal films with compression-resistant photoluminescence

Xiaobing Tang¹, Yulin Zhang¹, Nadeesha Lakmali Kothalawala², Xiyu Wen³, Doo Young Kim² and Fuqian Yang¹

E-mail: fuqian.yang@uky.edu

Received 19 December 2021, revised 25 February 2022 Accepted for publication 28 February 2022 Published 17 March 2022



Abstract

In this work, we develop an environmental-friendly approach to produce organic-inorganic hybrid MAPbBr₃ (MA = CH₃NH₃) perovskite nanocrystals (PeNCs) and PMMA-MAPbBr₃ NC films with excellent compression-resistant PL characteristics. Deionized water is used as the solvent to synthesize MAPbBr₃ powder instead of conventionally-used hazardous organic solvents. The MAPbBr₃ PeNCs derived from the MAPbBr₃ powder exhibit a high photoluminescence quantum yield (PLQY) of 93.86%. Poly(methyl methacrylate) (PMMA)-MAPbBr₃ NC films made from the MAPbBr₃ PeNCs retain \sim 97% and \sim 91% of initial PL intensity after 720 h aging in ambient environment at 50 °C and 70 °C, respectively. The PMMA-MAPbBr₃ NC films also exhibit compression-resistant photoluminescent characteristics in contrast to the PMMA-CsPbBr₃ NC films under a compressive stress of 1.6 MPa. The PMMA-MAPbBr₃ NC film integrated with a red emissive film and a blue light emitting source achieves an LCD backlight of \sim 114% color gamut of National Television System Committee (NTSC) 1953 standard.

Supplementary material for this article is available online

Keywords: organic-inorganic hybrid perovskite nanocrystals, deionized water, compression-resistant backlight films, display

(Some figures may appear in colour only in the online journal)

Introduction

Liquid crystal displays (LCDs) are one of dominant display technologies in contemporary world, with applications spanning smartphones, computer monitors, televisions (TVs), etc [1–3]. A backlight as a pivotal component of LCDs is usually

needed to illuminate the display panel. Currently, LCDs with a quantum-dot (QD) backlight have been developed and promoted over past years [4–8], which is based on the effect of quantum confinement and superior solution-processability.

The progress in the synthesis of lead halide perovskite QDs or nanocrystals (NCs), which are regarded as potential

¹ Materials Program, Department of Chemical and Materials Engineering, University of Kentucky, Lexington, KY 40506, United States of America

² Department of Chemistry, University of Kentucky, Lexington, KY 40506, United States of America
³ Center for Aluminum Technology, University of Kentucky, Lexington, KY 40506, United States of America

backlight materials, has led to rapid advancement and presented a great opportunity for next-generation lighting and displays due to their excellent brightness and color purity, high light-absorption coefficient, high defect tolerance, and cost-effective and facile preparation process [9]. Inorganic lead halide perovskites also possess good stability [10–13]. However, inorganic lead halide perovskites can experience phase transition [14-17] and photoluminescence (PL) shift under pressure [18], which can impede the applications of inorganic lead halide perovskites in backlights. This is because the PL nonuniformity of backlights from insufficient luminance in a local dimming zone can cause clipping effect [2]. There is a great need to find solutions to the pressureinduced PL shift and the clipping effect associated with mechanical stress/deformation for the applications of perovskites in flexible display.

There are reports that organic-inorganic hybrid perovskites can maintain a high color purity regardless of crystal size due to their intrinsic quantum-well-like structure [19, 20] in contrast to inorganic lead halide perovskites. For example, sandwiching a two-dimensional (2D) organic cation layer between 2D inorganic layers of metal halide octahedra forms a quantum-well-like structure from organic-inorganic hybrid perovskites [21]. Organic-inorganic hybrid perovskites with unique properties of extremely high optical absorption, small effective masses for electrons and holes, dominant point defects that only generate shallow levels, and grain boundaries that are essentially benign, have attracted great interest as promising materials (most notably CH₃NH₃(Pb,Sn)(I,Br)₃) (MA(Pb,Sn)(I,Br)₃)) for high-performance optoelectronic devices [20].

Currently, most methods for the preparation of lead halide perovskite nanocrystals (PeNCs) have involved the use of volatile-organic and toxic-organic solvents of octadecene (ODE) [22], dimethyl formamide (DMF) [23–26], dimethyl sulfoxide (DMSO) [23, 27] etc and are not environmentalfriendly for sustainable commercialization. Developing environmental-friendly methods for the synthesis of PeNCs is of practical importance to reduce harmful impacts to our planet. In addition to solution-based methods, there are solvent-free methods, which are also referred to solvent-free mechanochemical methods, available to synthesize PeNCs. These methods are mainly based on ball milling [28], which requires high energy and high stress to activate the reactions between different powders via the impact and attribution with hard balls made from steel and/or ceramics. The reactions are under high stress, and the impact and attribution likely introduce impurity from the hard balls to the MAPbBr₃ and CsPbBr₃ nanocrystals. It needs to be pointed out that organic solvents are needed for the storage of MAPbBr₃ and CsPbBr₃ nanocrystals, since they can experience coarsening and easily adsorb quenchers at room temperature. Recently, Lin et al [29, 30] demonstrated the feasibility to synthesize MAPbBr₃ and CsPbBr₃ microcrystals with deionized (DI) water and 2-methyl-imidazole. However, 2-methyl-imidazole is an organic compound, which is detrimental to the tissue of mucous membranes and upper respiratory tract [31], and experimental studies revealed that exposing rats to 2-methylimidazole can increase the rate of thyroid gland cancers and liver tumors [32]. Also, this method adds impurity (PbBr (OH)) in MAPbBr₃ microcrystals, which reduces the PLQY (photoluminescence quantum yield) of MAPbBr₃ powder and impairs carriers' transport for MAPbBr₃-based optoelectronic devices, leading to the performance degradation of the associated devices.

This work is targeting at the development of an environmental-friendly method to synthesize organic-inorganic hybrid MAPbBr₃ PeNCs (as shown schematically in figure 1) and investigate PL characteristics of poly(methyl methacrylate) (PMMA)-MAPbBr₃ NC films under compression instead of under bending in the study of the bending-endurable PL characteristics of PMMA-CsPbBr₃ NC films by Tang et al [33]. In contrast to conventional methods with environmentally hazardous solvents, such as ODE, DMF and DMSO, as the precursor solvent, we used deionized water as sole solvent in the production of MAPbBr₃ powder following the method developed by Tang et al [33] in the green preparation of CsPbBr3 powder. X-ray diffraction (XRD) was used to confirm cubic structure of the prepared MAPbBr₃ without any other crystals/impurities in contrast to the ball milling [28] and PbBr(OH) [29, 30] from the use of 2-methylimidazole. Organic-inorganic hybrid MAPbBr₃ PeNCs were derived from the prepared MAPbBr3 in toluene under ultrasonication. Using the MAPbBr₃ PeNCs, we constructed PMMA-MAPbBr₃ NC films as potential backlight films for LCDs. The photoluminescence quantum yield (PLQY) of the prepared MAPbBr₃ PeNCs reached 93.86%. The prepared PMMA-MAPbBr₃ NC films retained ~100% of initial PL intensity at 50 °C over a period of 30 d, demonstrating excellent thermal stability, and exhibited compression-resistant PL characteristics without significant change in the PL intensity under a compressive stress of 1.6 MPa or less.

Results and discussion

Figure 1 presents a schematic for the production of MAPbBr₃ NCs, which consists of two steps. The first step focuses on the synthesis of MAPbBr₃ powders. A suitable amount of water was added into a glass vial with equimolar MABr and PbBr₂ precursor powders, leading to the formation of white precipitates (figure S1 (available online at stacks.iop.org/NANO/33/235605/mmedia), supporting information). A layer of the white precipitates was heated on a hot plate at 40 °C for 30 min. The heating of these white precipitates resulted in the formation of orange powders, which emit green light under UV irradiation (figure S2, supporting information).

The XRD spectra of the orange MAPbBr₃ powders (figure S3, supporting information) reveals the (100), (110), (200), (210), (211), (220) and (300) crystal planes of MAPbBr₃ crystal of cubic phase [34, 35]. The reactions responsible for the formation of MAPbBr₃ crystals are illustrated as below.

$$MABr(s) + PbBr_2(s) \rightarrow MA^+(aq) + Pb^{2+}(aq) + 3Br^-(aq)$$
 (1)

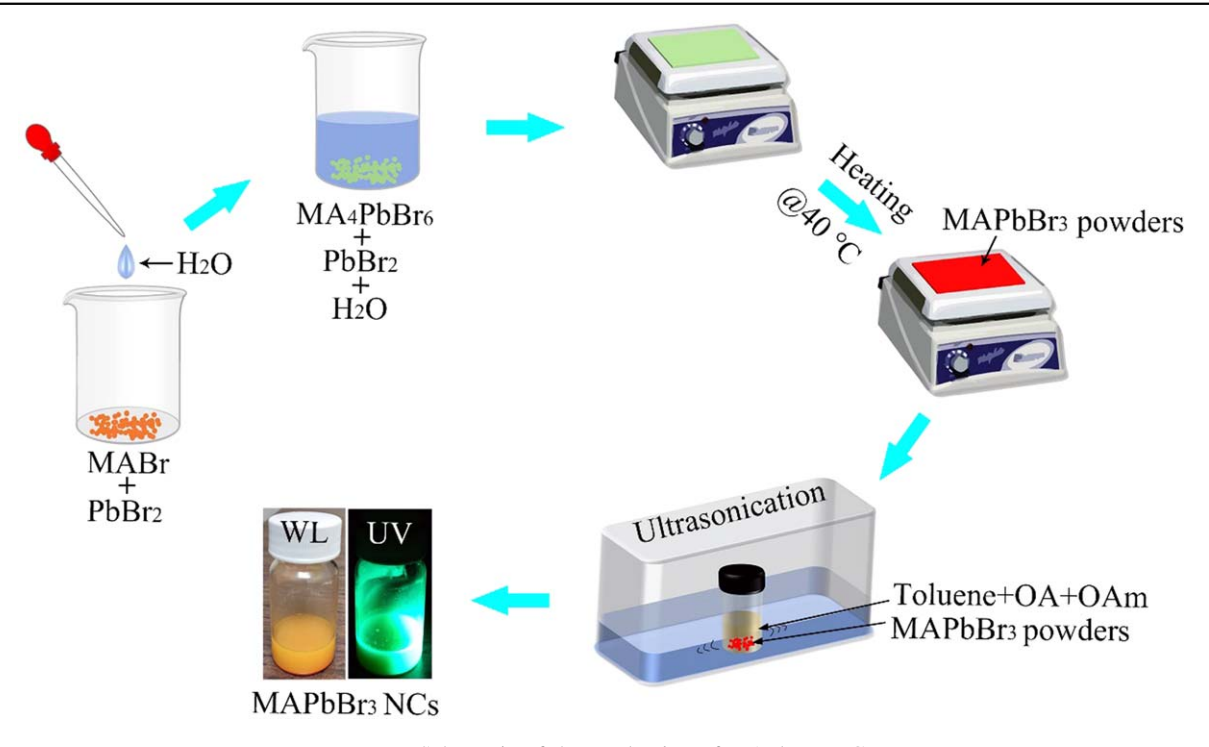


Figure 1. Schematic of the production of MAPbBr₃ NCs.

$$MA^{+}(aq) + Pb^{2+}(aq) + 3Br^{-}(aq) \rightarrow MAPbBr_{3}(s)$$
 (2)

$$MAPbBr_3(s) + 3MABr(s) \rightarrow MA_4PbBr_6(s)$$
 (3)

$$MA_4PbBr_6(s) + 3PbBr_2(s) \stackrel{40 \circ C}{=} 4MAPbBr_3(s).$$
 (4)

First, MABr reacts with $PbBr_2$ in DI water at room temperature to form orange MAPbBr₃ immediately (equations (1) and (2), figure S1(a) in supporting information). Note that the solubility of MABr in water is much larger than $PbBr_2$ in water at room temperature (figure S4 in supporting information). The orange MAPbBr₃ precipitates react further with MABr in DI water to produce white precipitates of MA_4PbBr_6 [36] (equation (3), figure S1(b) in supporting information), and $PbBr_2$ residual precipitates in DI water.

Heating the resultant precipitates, which consist of MA₄PbBr₆ and PbBr₂, at 40 °C produces MAPbBr₃ powders (crystals of cubic phase) (figure S3), similar to the reaction reported by Akkerman *et al* [37]. The as-obtained MAPbBr₃ powders emit strong green light under ultraviolet (UV) light (365 nm in wavelength, same hereinafter).

In the second step, the as-obtained MAPbBr₃ powders were placed in a suspension, which consisted of toluene and ligands of oleic acid (OA) and oleylamine (OAm). The as-obtained MAPbBr₃ powders in the toluene suspension were subsequently exposed to ultrasonic wave in an ultrasonic bath to produce MAPbBr₃ PeNCs. The ultrasonic wave exerted radiation force on the MAPbBr₃ powders in the suspension and caused breakage of the MAPbBr₃ powders to MAPbBr₃ crystals of nano-sizes through the formation and growth of cracks [38]. Such a process leads to the production of MAPbBr₃ PeNCs in toluene.

Figure 2(a) presents TEM (transmission electron microscopy) and HRTEM (high resolution transmission electron

microscopy) images of MAPbBr₃ PeNCs and the energydispersive spectroscopy (EDS) mapping of Pb and Br. The specimen for the TEM analysis was from the supernatant of an as-obtained NC solution after centrifugation at 8000 rpm for 5 min. The size distribution of the MAPbBr₃ NCs from the TEM image is presented in figure S5 (supporting information), revealing that the average size of the MAPbBr₃ NCs is \sim 5 nm; the lattice spacing is measured to be \sim 0.294 nm from the HRTEM image, corresponding to (200) crystal plane [35]. Both Pb and Br are presented in the specimen, as shown in the EDS mapping. Figure S6 in supporting information presents the EDS spectrum of the prepared MAPbBr₃ nanocrystals, and table S1 in supporting information summarizes elemental information. According to table S1, the atomic ratio of Pb to Br is \sim 1:3 in good accord with the stoichiometric ratio of Pb to Br in MAPbBr₃, confirming the formation of MAPbBr₃. Note that the element C presented in the EDS spectrum is from the carbon film on the copper grid holder for the TEM imaging and the specimen. The element N is from the ligands (OA and OAm) and CH₃NH₃- ions, and the element Cu is from the copper grid holder.

The XRD pattern of the MAPbBr₃ NCs from the supernatant of an as-obtained NC solution after centrifugation at 8000 rpm for 5 min (figure 2(b)) reveals cubic phase of MAPbBr₃ PeNCs in agreement with the EDS analysis from figure 2(a). There are three peaks centered at 14.97°, 30.08° and 33.8° corresponding to the (100), (200) and (210) crystal planes of cubic CsPbBr₃, respectively, according to the PDF#54-0752 and the report given by Schmidt *et al* [35]. Using the Scherrer equation ($D = K\lambda/\beta\cos\theta$; D, K, λ , β and θ are average crystallite size, shape factor, wavelength of x-ray, half width and diffraction angle of the XRD peak, respectively) for the MAPbBr₃ NCs from the supernatant, we

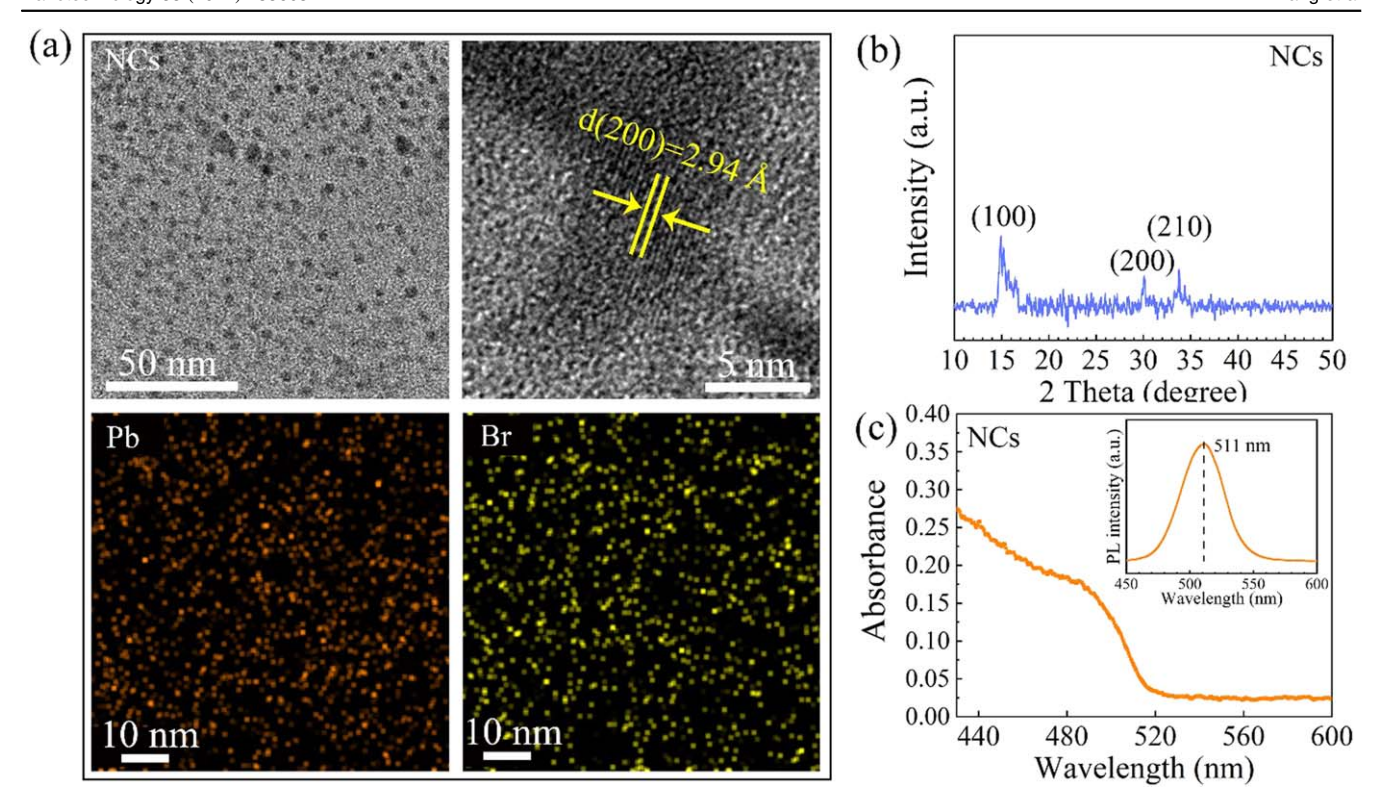


Figure 2. Characteristics of MAPbBr₃ PeNCs: (a) TEM image (upper-left corner), HRTEM image (upper-right corner) and EDS mapping (bottom) of Pb and Br, (b) XRD pattern in consistence with the PDF card#54-0752, and (c) UV-vis absorbance and PL spectrum (inset). The specimen for the TEM and XRD analyzes was from the supernatant of an as-obtained NC solution after centrifugation at 8000 rpm for 5 min.

estimate the average size of the MAPbBr3 NCs to be \sim 5 nm, comparable to that from figures 2(a) and S5. The sonication of MAPbBr₃ powders in the toluene suspension did not cause any phase change to the MAPbBr₃ crystals. The UV-vis absorption spectrum in figure 2(c) shows that the MAPbBr₃ NC solution has a strong absorbance at ~488 nm, and the PL spectrum (inset of figure 2(c)) demonstrates the green emission of the MAPbBr₃ NC solution at 511 nm. The PLQY of the MAPbBr₃ NCs in toluene reached 93.86%. It is worth mentioning that different excitation lights can produce different values of PLQY. Two excitation lights with wavelengths of 365 nm and 390 nm were used to determine the PLQY of the MAPbBr₃ NCs in toluene, and table S2 (supporting information) summarize the results. The average PLQY under an excitation wavelength of 365 nm is 93.86%, higher than 90.60% under an excitation wavelength of 390 nm. Such a difference can be attributed to that the shorter the wavelength, the higher is the energy of a photon, likely resulting in the generation of multiple excitons, i.e., one photon of a high energy can produce multiple photons and excitons [39].

We prepared a suspension by mixing the MAPbBr₃ PeNCs in a PMMA ($M_W = 35000$) (Fisher Scientific, Pittsburgh, PA) solution with toluene as solvent and coated a layer of the suspension on the surface of polyethylene terephthalate (PET) substrates ($2.5 \times 2.5 \times 0.08$ cm³ in dimensions) to produce polymer composite films consisting of a PMMA matrix and MAPbBr₃ PeNCs dispersed in the PMMA matrix. The films,

which are referred to as PMMA-MAPbBr₃ NC films, were used as backlight films in ultrawide color gamut LCD.

Figure 3(a) depicts an optical image of a PMMA-MAPbBr $_3$ NC film on a PET under UV light. There was green emission from the film. From the optical image of the cross-section of a PMMA-MAPbBr $_3$ NC film in figure 3(a), the thickness of the PMMA-MAPbBr $_3$ NC film is estimated to be 18.57 \pm 0.69 μ m.

Figure 3(b) shows the UV-vis absorbance (blue line) and PL (coffee line) spectra of the PMMA-MAPbBr₃ NC films, which exhibit absorption and PL peaks at 517 and 523 nm, respectively. The difference between the PL and absorbance peaks yields a small Stokes shift of 6 nm, indicating the presence of reabsorption loss [40], i.e. a significant overlap of absorption and photoluminescence spectra can cause remarkable reabsorption, leading to a lower band to band emission. Note that the Stokes shift corresponds to an exciton binding energy [41]. The Stokes shift of 6 nm yields an exciton binding energy of 27.5 meV, which is comparable to the thermal energy $(k_BT; k_B \text{and } T \text{ are the Boltzmann constant})$ and absolute temperature, respectively) of 25.9 meV at room temperature, resulting in moderate light emission due to the dissociation of photogenerated carriers [42] and the decrease of number of electron-hole pairs. Such a small difference between 27.5 meV and 25.9 meV suggests that the PMMA reduces the number of emitted photons, as supported by the PLQY of 13.12% for the PMMA-MAPbBr₃ NC films.

The absorbance spectra of the PET, PET/PMMA (PMMA coated on PET) and glass/PMMA (PMMA coated

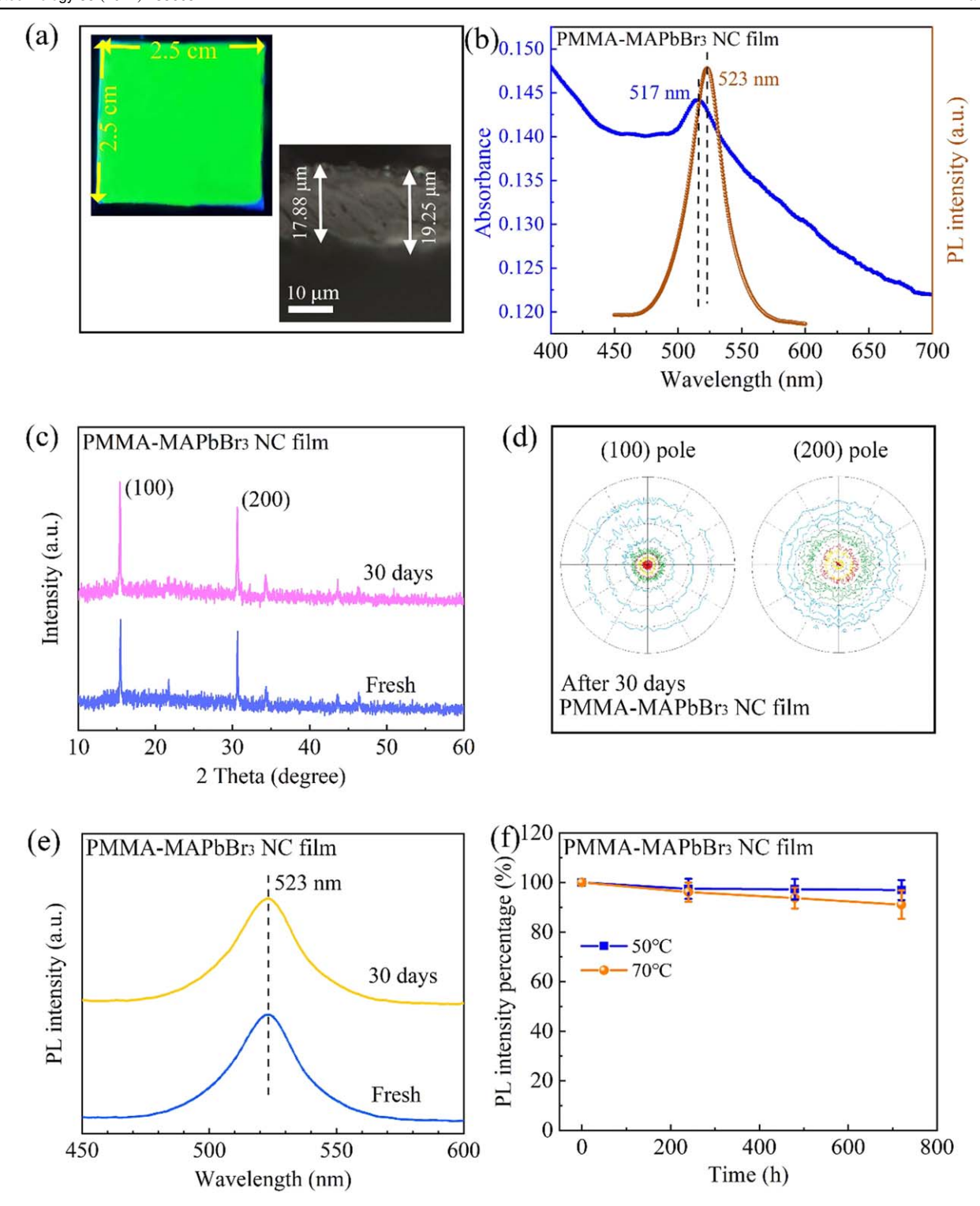


Figure 3. (a) Optical images of a PMMA-MAPbBr₃ PeNC film on a PET substrate (2.5 × 2.5 cm²) under UV light (upper-left corner) and cross-section of the PMMA-MAPbBr₃ PeNC film, (b) UV–vis absorbance (blue line) and PL (coffee line) spectra of PMMA-MAPbBr₃ PeNC films, (c) XRD patterns of a fresh PMMA-MAPbBr₃ PeNC film (blue line) and the same film placed in ambient environment for 30 d (magenta line), (d) pole figures for (100) and (200) planes of the PMMA-MAPbBr₃ PeNC film placed in ambient environment for 30 d, (e) PL spectra of the fresh PMMA-MAPbBr₃ PeNC film (blue line) and the same film placed in ambient environment for 30 d (yellow line), and (f) temporal evolution of the PL intensities of the PMMA-MAPbBr₃ PeNC films at 50 °C (80% relative humidity (RH)) and 70 °C (80% RH) over a period of 30 d. Error bars stand for standard deviation of the percentage of PL intensity.

on glass) are presented in figure S7 in supporting information. It is evident that both the PET and PET/PMMA exhibit long Urbach tail in the absorbance spectra and the glass/PMMA does not. This result reveals that the long Urbach tail presented in figure 3(b) is due to the strong absorbance from the PET substrate.

We use the temporal evolution of the XRD pattern and PL characteristics to examine the structural and optical stabilities of the PMMA-MAPbBr₃ NC films. Figure 3(c) presents the XRD patterns of a fresh PMMA-MAPbBr₃ NC film and the same PMMA-MAPbBr₃ NC film placed in ambient environment (21.0 °C and 80% RH) for 30 d, respectively. There are two dominant peaks corresponding to the (100) and (200) planes of the MAPbBr₃ PeNCs. There is no observable difference between the XRD patterns, indicating no phase transformation and dissociation of the MAPbBr₃ PeNCs. Such a result suggests excellent structural stability of the PMMA-MAPbBr₃ NC films.

Figure 3(d) presents the X-ray pole figures ((100) pole and (200) pole) of a PMMA-MAPbBr₃ NC film. The larger and darker spot at the center of (100) pole figure than that at (200) pole figure reveals a stronger orientation of (100) plane than (200) plane, corresponding to the results in figure 3(c). Such a result indicates that the MAPbBr₃ NCs with the orientation on (100) crystal plane have more 'uniform and ideal' growth along $\langle 100 \rangle$ direction than (200) crystal plane. Note that the (100) plane is different from the (200) plane due to atomic difference—the (100) plane consists of MA (CH₃NH₃⁺) and Br⁻, and the (200) plane consists of Br⁻ and Pb²⁺.

Figure 3(e) depicts the PL spectra of a fresh PMMA-MAPbBr₃ NC film and the same PMMA-MAPbBr₃ NC film placed in ambient environment (21.0 °C and 80% RH) for 30 d, respectively. There is a PL peak centered at 523 nm for both films, and no PL shift is observed. The peak intensity remains nearly unchanged for the period of 30 d in ambient environment. Such results are in good accord with the absorbance results (figure S8, supporting information), in which the absorption peak and intensity remain unchanged over the same period.

For comparison, MAPbBr₃ NCs were coated on a PET substrate to form a layer of MAPbBr₃ NC film. Figure S9 in supporting information depicts the PL spectra of the MAPbBr₃ NC film over a period of 240 h. There are no peak shift and intensity change, suggesting a good optical stability of the MAPbBr₃ NCs in ambient environment. Note that there is a red shift of 2 nm between the MAPbBr₃ NC film and the MAPbBr₃ NCs in a toluene solution, which might be due to the agglomeration of MAPbBr₃ NCs in the film.

Figures 3(f) and S10 (supporting information) summarize the temporal evolution of the PL peak intensity and PL wavelength of the PMMA-MAPbBr₃ NC films in air of 80% RH at 50 °C and 70 °C, respectively, over a period of 720 h. There is no observable shift in the PL wavelength. The PMMA-MAPbBr₃ NC films retained \sim 97% and \sim 91% of the initial PL intensity after 720 h aging at 50 °C and 70 °C respectively with a standard deviation of \sim 4% and \sim 6%, respectively, as indicated by the error bars. The results

indicate that the PMMA-MAPbBr₃ NC films possess outstanding optical and thermal stabilities, which can be attributed to the interaction between PMMA chains and the ligands on the surfaces of MAPbBr₃ PeNCs. The strong interaction between PMMA chains and the ligands forces the ligands onto the MAPbBr₃ PeNCs, which reduces the surface trap density of the MAPbBr₃ NCs and stabilizes the photoelectronic performance of the MAPbBr₃ NCs. Note that the separation of the ligands from MAPbBr₃ NCs increases the density of trap states, resulting in inferior optical performance [9, 43, 44].

The density of trap states can be analyzed from the lifetime of photogenerated charge carriers. The longer the lifetime, the less is the density of trap states due to the decrease in nonradiative recombination [45]. Here, the photogenerated carrier's lifetime of the MAPbBr₃ PeNCs was evaluated from the time-resolved PL decays [46] at the excitation wavelength of 390 nm at room temperature. Figure S11(a) in supporting information shows the time correlated single photon counting (TCSPC) curve of the prepared MAPbBr₃ PeNCs. For comparison, the TCSPC curve of the PMMA-MAPbBr₃ NC films is presented in figure S11(b) (supporting information). Using a bi-exponential function with a shorter decay component, τ_1 , and a longer decay component, τ_2 [46], which correspond to the interactive state (surface) and non-interactive state (core) of the samples, respectively [47–49], to curve-fit both curves, we obtain the longer decay components of 35.5 ns and 9931.8 ns for the MAPbBr₃ NCs and PMMA-MAPbBr₃ NC films, respectively, and the shorter decay components of 8.2 ns and 12.5 ns for the MAPbBr₃ NCs and PMMA-MAPbBr₃ NC films, respectively, as shown in figures S11(c) and (d) (supporting information). The significant increase in both the longer and shorter decay components in the PMMA-MAPBBr3 NC films clearly suggest the suppression of nonradiative recombination channels. This is because the PMMA layer prevents the diffusion of quencher molecules, such as oxygen molecules [50] and moisture [51], to MAPbBr₃ NCs.

The effect of the excitation-light power on the lifetime of both the MAPbBr₃ NCs and PMMA-MAPbBr₃ NC films was examined. Table S3 in supporting information summaries the lifetimes of the MAPbBr₃ NC films and PMMA-MAPbBr₃ NC films under the irradiation of UV light of different powers. For the MAPbBr₃ NCs, there are no statistically significant differences between the longer decays and between the shorter decays for the power of the excitation light in a range of 32%-100% of the incident light. For the PMMA-MAPbBr₃ NC films, there is no statistically significant difference between the shorter decays for the power of the excitation light in a range of 32%–100% of the incident light, while there is about \sim 50 ns difference of the longer decays between the excitation light with a power in a range of 79%-100% of the incident light and that with a power in a range of 32%–50% of the incident light. However, \sim 50 ns is much smaller that \sim 9900 ns of the longer decays for the PMMA-MAPbBr₃ NC films. Thus, the power of the excitation light has no significant effect on the decay times of both films.

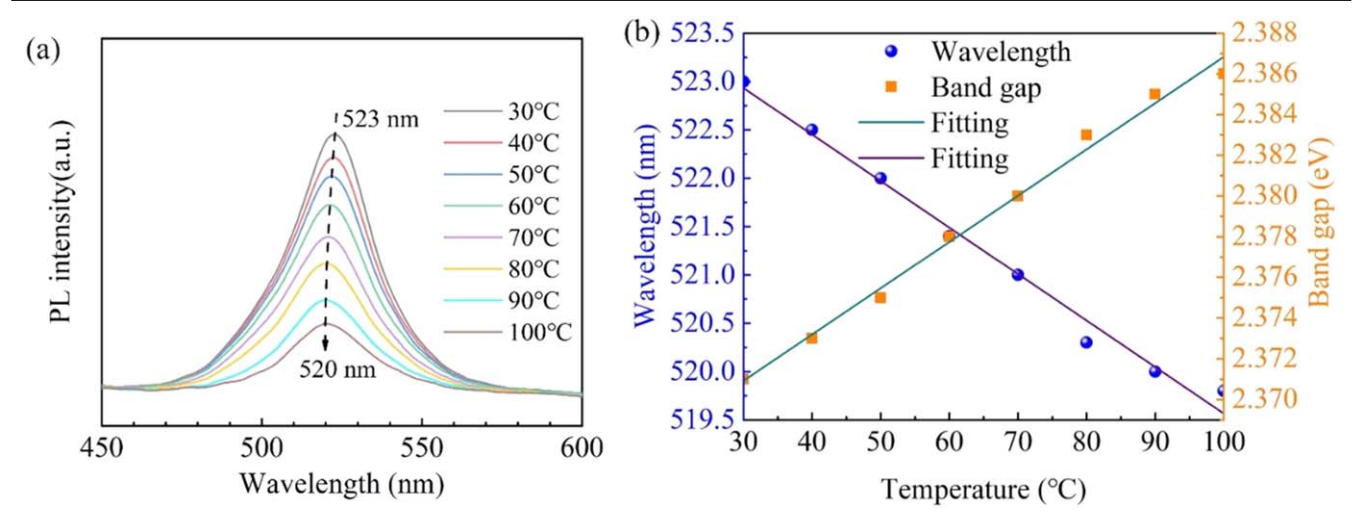


Figure 4. (a) PL spectra of the PMMA-MAPbBr₃ NC films at different temperatures, and (b) temperature dependence of PL wavelength (blue ball) and band gap (brown square).

Note that the PMMA-MAPbBr₃ NC films in air of 80% RH at 70 °C experienced a marginal decline in the PL intensity and retained ~91% of the initial PL intensity over 720 h (figure 3(f)). The temperature increase from 50 °C to 70 °C intensifies the activities of phonons (absorption and/or emission) of the MAPbBr₃ NCs, which enhances the non-radiative generation-recombination (Hall–Shockley–Read (HSR)) processes [52, 53], as illustrated in figure S12 in supporting information.

The effect of temperature on the PL characteristics of the PMMA-MAPbBr₃ NC films was investigated in a temperature range of 30 °C–100 °C, as shown in figure 4. The PL peak experienced a blue shift (the wavelengths change from long wavelength to short wavelength, and the band gap changes in an opposite trend), suggesting the increase of the bandgap of the MAPbBr₃ PeNCs with increasing temperature. Simultaneously, the PL intensity decreased with the increase of temperature due to the dissociation of excitons and the intensifying phonon activities [52–54].

To the first-order approximation, the bandgap of a semiconductor nanocrystal at stress-free state as a function of the temperature change can be expressed as [55]

$$E(T) = E(T_0) + \alpha_T \Delta T \tag{5}$$

for $|\Delta T|/T_0 \ll 1$. Here, E is the bandgap of the semi-conductor nanocrystal, T_0 is a reference temperature, T is temperature, and ΔT is the temperature change. The parameter α_T , which represents the dependence of bandgap on temperature, is calculated as

$$\alpha_T \equiv \frac{\partial E}{\partial T} \bigg|_{T = T_{0,D}}.$$
 (6)

There are two contributions to the temperature dependence of bandgap—one is from thermal expansion and the other is from electron–phonon interaction [56]. Assuming that the coupling between the effect of thermal expansion and the electron–phonon interaction is negligible, we can express α_T

as [57]

$$\alpha_T = \left(\frac{\partial E}{\partial V} \cdot \frac{\partial V}{\partial T}\right) \bigg|_{T = T_0, p} + \left. \frac{\partial E}{\partial T} \right|_{T = T_0, e - p} \tag{7}$$

in which the second term represents the contribution of the electron–phonon interaction [57]. Here, $(\partial V/\partial T)_{T=T0,p}$ is proportional to the coefficient of thermal expansion, and $(\partial E/\partial V)_{T=T0,p}$ represents the bandgap change with the volume of the semiconductor nanocrystal.

According to figure 4(b), the bandgap of the MAPbBr₃ NCs is approximately a linearly increasing function of temperature, which supports the linear relationship between the bandgap and the temperature change in equation (5) and reveals $\alpha_T > 0$. Keshavarz *et al* [58] reported 0.67 K⁻¹ for the coefficient of thermal expansion of MAPbBr₃, suggesting the increase of the volume of MAPbBr₃ nanocrystals with the increase of temperature. For semiconductor nanocrystals, the bandgap decreases with the increase of the nanocrystal size due to the quantum-confinement effect, i.e. $(\partial E/\partial V)_{T=T0,p} < 0$. Thus, it requires $(\partial E/\partial T)_{T=T0,e-p} > 0$. The electrophonon interaction in the MAPbBr₃ PeNCs widens the bandgap with the increase of temperature.

It is known that the bandgap of a semiconductor is inversely proportional to the emission wavelength, i.e. $E = hc/\lambda$ (h, c, and λ are the Planck constant, light speed in vacuum and emission wavelength of photon, respectively). According to equation (5), the emission wavelength of the MAPbBr₃ NCs, λ , is also a function of temperature. To the first-order approximation, we also have

$$\lambda(T) = \lambda(T_0) + \beta_T \Delta T \tag{8}$$

for $|\Delta T|/T_0 \ll 1$. Using equations (5) and (8) to fit the experimental results in figure 4, we obtain $(E(T_0), \lambda(T_0))=(2.371 \, \text{eV}, 522.9 \, \text{nm})$ and $(\alpha_T, \beta_T)=(2.3 \times 10^{-4} \, \text{eV} \, \text{K}^{-1}, -0.047 \, \text{nm} \, \text{K}^{-1})$. Using the numerical values of $E(T_0), \lambda(T_0), \alpha_T$ and β_T , we note $E(T_0) = hc/\lambda(T_0)$ and $E(T_0)\beta_T = -\lambda(T_0)\alpha_T$ in accord with $E = hc/\lambda$.

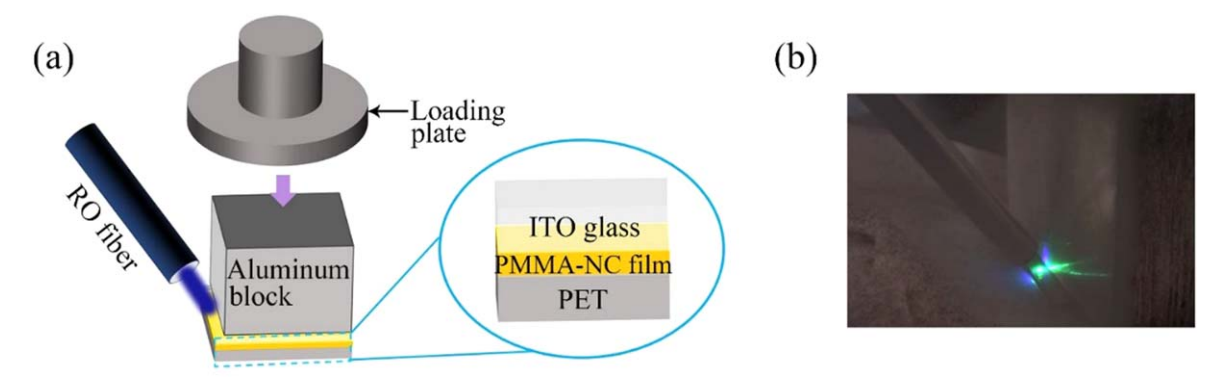


Figure 5. (a) Schematic of experimental setup of the PL test of PMMA-NC films under compression, and (b) optical image of the system in a dark environment.

It is known that the temperature dependence of the intensity of the emission light can be expressed as [59]

$$I(T) = \frac{I_0}{1 + Ae^{(-E_A/k_BT)}},\tag{9}$$

where I(T) and I_0 are the PL intensities at temperature T and 0 K, respectively, E_A and k_B are activation energy (also referred to as exciton binding energy in some literatures [60, 61]) and Boltzmann's constant, respectively, and A is a constant. Figure S13 in supporting information shows the temperature dependence of the intensity of the PL peak for the PMMA-MAPbBr₃ NC films. Using equation (9) to curve-fit the data in figure S13, we obtain $E_A = 478$ meV. For comparison, the fitting curve is also included in figure S13. Note that there is a large difference between 478 meV calculated from figure S13 and 27.5 meV obtained from the Stokes shift. Such a large difference indicates that the 478 meV is likely not the exciton binding energies of the MAPbBr₃ NCs.

The exciton binding energies of bulk and nanocrystal MAPbBr₃ are 84 ± 10 meV and 320 ± 100 meV, respectively, as reported by Zheng *et al* [62] in the temperature range of -33 °C to 77 °C. There also exist large differences between 27.5 meV obtained from the Stokes shift and the exciton binding energies of bulk and nanocrystal MAPbBr₃ reported by Zheng *et al* [62], which again suggest that 478 meV obtained from equation (9) and figure S13 likely is not the exciton binding energy of the NCs in PMMA-NC films. It should be noted that the 478 meV obtained from the temperature dependence of the PL intensity is close to the upper bound of 420 meV reported by Zheng *et al* [62].

It is known that there likely exist two processes controlling the temperature dependence of the intensity of emitting light: one is associated with the delocalization of excitons and the other is associated the thermal quenching of luminescence. Under such a case, the temperature dependence of the intensity of the emission light needs to be expressed as [63–65]

$$I(T) = \frac{I_0}{1 + Ae^{(-E_1/k_BT)} + Be^{(-E_2/k_BT)}}. (10)$$

Here, E_1 and E_2 represent the exciton binding energy [64] and the activation energy for thermal quenching [63], respectively, and A and B are constants. Using equation (10) to fit

the date in figure S13, we can determine E_1 and E_2 . The fitting curve is depicted in figure S14, and the fitting equation is presented in equation (11) as below

$$I(T) = \frac{7.9 \times 10^3}{1 + 0.79e^{-2.61/RT} + 137.62 \times 10^4 \times e^{-40/RT}}.$$
(11)

The numerical values of E_I and E_2 are $2.61 \,\mathrm{kJ}\,\mathrm{mol}^{-1}$ (27.0 meV) and $40 \,\mathrm{kJ}\,\mathrm{mol}^{-1}$ (415 meV), respectively. Here, R is the gas constant. The exciton binding energy of the MAPbBr₃ NCs in the PMMA-NC films is 27.0 meV, in good agreement with the one (27.5 meV) obtained from Stokes shift (figure 3(b)). The activation energy for thermal quenching is 415 meV. Comparing the numerical values of A and B, we note $A \ll B$. Such a result reveals that thermal quenching of luminescence is the dominant process controlling the loss of the PL intensity at high temperature.

Figure 5(a) shows a schematic of the experimental setup used to examine the change in the PL characteristics of a PMMA-MAPbBr3 NC film on a PET substrate under compression. An ITO (Indium Doped Tin Oxide) coated glass $(2.5 \times 2.5 \text{ cm}^2)$ was placed on the surface of the PMMA-MAPbBr₃ NC film to form a sandwich-like structure. The compression of the sandwich-like structure, which was placed between an aluminum block and a stainless-steel block, was performed at room temperature on a universal Testing Machine (ESACU200, Shimadzu, Japan). A reflective optical (RO) probe was used to record the PL spectrum, as shown in figure S15 in supporting information. There are two aspects for the use of the ITO glass. First, ITO glass, which is much stiffer than the PMMA-MAPbBr₃ NC film and have a 'smooth' surface, allows relatively uniform compression on the PMMA-MAPbBr₃ NC film. Secondly, ITO glass has a good light-admitting quality, allowing the laser from the RO probe to reach the PMMA-MAPbBr₃ NC film. Figure 5(b) presents an optical image of the green emission of the PMMA-MAPbBr₃ NC film under compression in a dark environment, demonstrating that the MAPbBr₃ NCs can emit green light under compression.

For comparison, a set of PMMA-CsPbBr₃ NC films on PET substrate with approximately the same geometrical configuration were also prepared, in which the all-inorganic

CsPbBr₃ NCs were synthesized by an antisolvent method. The PL characteristics of the PMMA-MAPbBr₃ NC films on PET substrate under the same compression conditions were examined.

Figures 6(a)–(d) presents the PL characteristics of the PMMA-MAPbBr₃ NC films under the action of compressive stress. It is evident that there is no shift in the PL peak (523 nm), suggesting that the compressive stress of 1.6 MPa or less has no effect on the bandgap of the MAPbBr₃ NCs dispersed in the PMMA matrix. The PL peak intensity of the PMMA-MAPbBr₃ NC film experienced slight decrease with the increase of compressive stress (figures 6(a), (b)), and the PL peak intensity of the PMMA-MAPbBr₃ NC film under the compressive stress of 1.6 MPa is ~90.5% of the initial peak intensity. There is only a $\sim 9.5\%$ (0.47% in standard deviation) decrease in the PL peak intensity (figure 6(b)). Figures 6(c), (d) depicts the temporal evolution of the PL characteristics of the PMMA-MAPbBr3 NC films under the compressive stress of 1.6 MPa. No PL shift is observed in the period of 6 min (figure 6(c)). The PL peak intensity experienced a slight increase of $\sim 0.4\%$ (0.9% in standard deviation) of the initial PL peak intensity under the compression for 6 min (figure 6(d)). Note that there is a shoulder at \sim 545 nm in the PL spectra shown in figure 6(a). The presence of the shoulder might be due to the defects on the surfaces of the MAPbBr₃ NCs since no shoulder is present under the compressive stress of 1.6 MPa. The large compressive stress enhances the interaction between PMMA and the MAPbBr₃ NCs, leading to the disappearance of the defect-related PL shoulder (figure 6(c)).

Figures 6(e)–(h) depicts the PL characteristics of the PMMA-CsPbBr₃ NC films under the action of compressive stress. Similar to the PMMA-MAPbBr3 NC films, the PMMA-CsPbBr₃ NC films did not experience PL shift (525 nm) under compressive stress for the compressive stress less than or equal to 1.6 MPa (figure 6(e)). In contrast to the PMMA-MAPbBr₃ NC films, the PL peak intensity of the PMMA-CsPbBr₃ NC films increased nonlinearly with the increase of compressive stress. There is a $\sim 56.8\%$ (2% in standard deviation) increase in the PL intensity under the compressive stress of 1.6 MPa (figure 6(f)). Figures 6(g), (h) shows the temporal evolution of the PL characteristics of the PMMA-CsPbBr₃ NC films under the action of 1.6 MPa. No PL shift is observed in the period of 6 min (figure 6(g)). The PL peak intensity experienced a ~10% (1% in standard deviation) increase after the compression for 1 min and 14% (2% in standard deviation) for 6 min (figure 6(h)).

Comparing the results shown in figures 6(b) and (d) to those in figures 6(f) and (h), we can conclude that the effects of compressive stress on the PL characteristics of the PMMA-MAPbBr₃ NC films are different from those on the PMMA-CsPbBr₃ NC films. These results illustrate that the PMMA-MAPbBr₃ NC films likely have potential applications as compression-resistant LCD backlight to mitigate the clipping effect due to the PL nonuniformity of backlights from insufficient luminance in a local dimming zone under

compression. However, the increase of the PL intensity of the PMMA-CsPbBr₃ NC films with the increase of the compressive stress indicates that PMMA-CsPbBr₃ NC films are more suitable than PMMA-MAPbBr₃ NC films in the application for a down converter because an enhanced PL intensity is required for a down converter [66].

It needs to be pointed out that the mechanisms for such a difference are unclear and might be due to the difference in cations (MA⁺ and Cs⁺), which likely have different interactions with PMMA chains. MA⁺ likely has a stronger interaction with PMMA than Cs⁺, resulting in stronger passivation of PMMA on MAPbBr3 NCs than that on CsPbBr₃ NCs. Under compression, the increase in the interaction between PMMA and CsPbBr₃ NCs is larger than that between PMMA and MAPbBr3 NCs, leading to more significant passivation of PMMA on CsPbBr3 NCs than on MAPbBr₃ NCs. Once the passivation is enhanced, the trapstate density decreases and the PL intensity increases. Note that there are other factors, which can contribute to the difference in the change of the PL peak intensity, such as the size of NCs and stress state. From the TEM image of the CsPbBr₃ NCs shown in figure S16 in supporting information, we obtain an average size of $\sim 11 \text{ nm}$ for the CsPbBr₃ NCs, which is in accord with the XRD result in figure S17 (supporting information) and smaller than $\sim 23 \text{ nm}$ of the MAPbBr₃ NCs used in the PMMA-MAPbBr₃ NC films, as calculated from the XRD pattern (figure S18 and table S4 in supporting information).

There are two mechanisms contributing to the photo emission of PeNCs—one is associated with core emission, and the other is related to surface emission. Surface emission possesses a shorter PL decay than core emission since surface sites are more accessible to quenchers for non-radiative recombination. PL intensity is the product of the photon emission rate at each site and the density of emissive sites [67]. Assume that the number of surface emissive sites is sensitive to compression and core sites is unaffected. The smaller the semiconductor nanocrystal, the more is the surface sites per unit volume available for the photon emission, and the larger is the PL intensity. Thus, there are more surface sites for the CsPbBr₃ NCs than the MAPbBr₃ NCs. Under compression, more surface sites per unit volume are likely activated, leading to the increase of the PL peak intensity. Also, the difference in the enhancement of photon transitions under compression in PMMA matrix can contribute to the difference of the photo emission in the response to compression between the CsPbBr₃ NCs and the MAPbBr₃ NCs [68].

The PMMA-MAPbBr₃ NC films were used to construct a light structure, which consisted of a red-emissive film (599 nm in emission wavelength) (figure S19 in supporting information), a green-emissive PMMA-MAPbBr₃ NC film and a blue light source, to mimic LCD backlight, as shown in figure 7(a). A blue light-emitting diode (450 nm) was used as the light source, and an optical fiber was used to receive optical signal from the 'backlight'. Figure 7(b) shows an

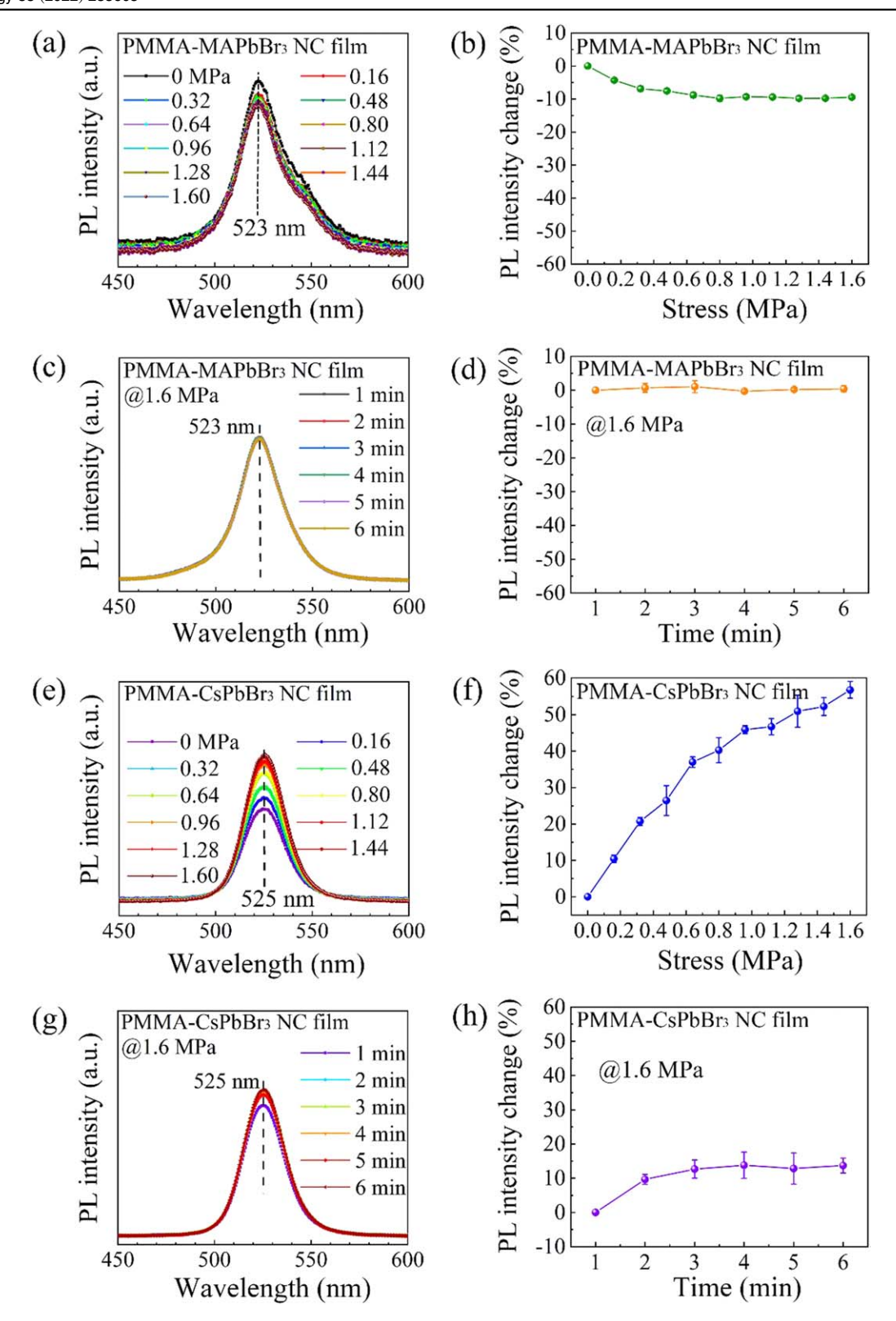


Figure 6. (a) PL spectra of a PMMA-MAPbBr₃ NC film under different compressive stresses, (b) variation of the PL peak intensity of the PMMA-MAPbBr₃ NC film with compressive stress, with error bars representing the standard deviation of the PL intensity change (same hereinafter), (c) PL spectra of the PMMA-MAPbBr₃ NC film under a compressive stress of 1.6 MPa at different instants, (d) temporal evolution of the PL peak intensity of the PMMA-MAPbBr₃ NC film under a compressive stress of 1.6 MPa, (e) PL spectra of a PMMA-CsPbBr₃ NC film under different compressive stresses, (f) variation of the PL peak intensity of the PMMA-CsPbBr₃ NC film with compressive stress, (g) PL spectra of the PMMA-CsPbBr₃ NC film under a compressive stress of 1.6 MPa at different instants, and (h) temporal evolution of the PL peak intensity of the PMMA-CsPbBr₃ NC film under a compressive stress of 1.6 MPa.

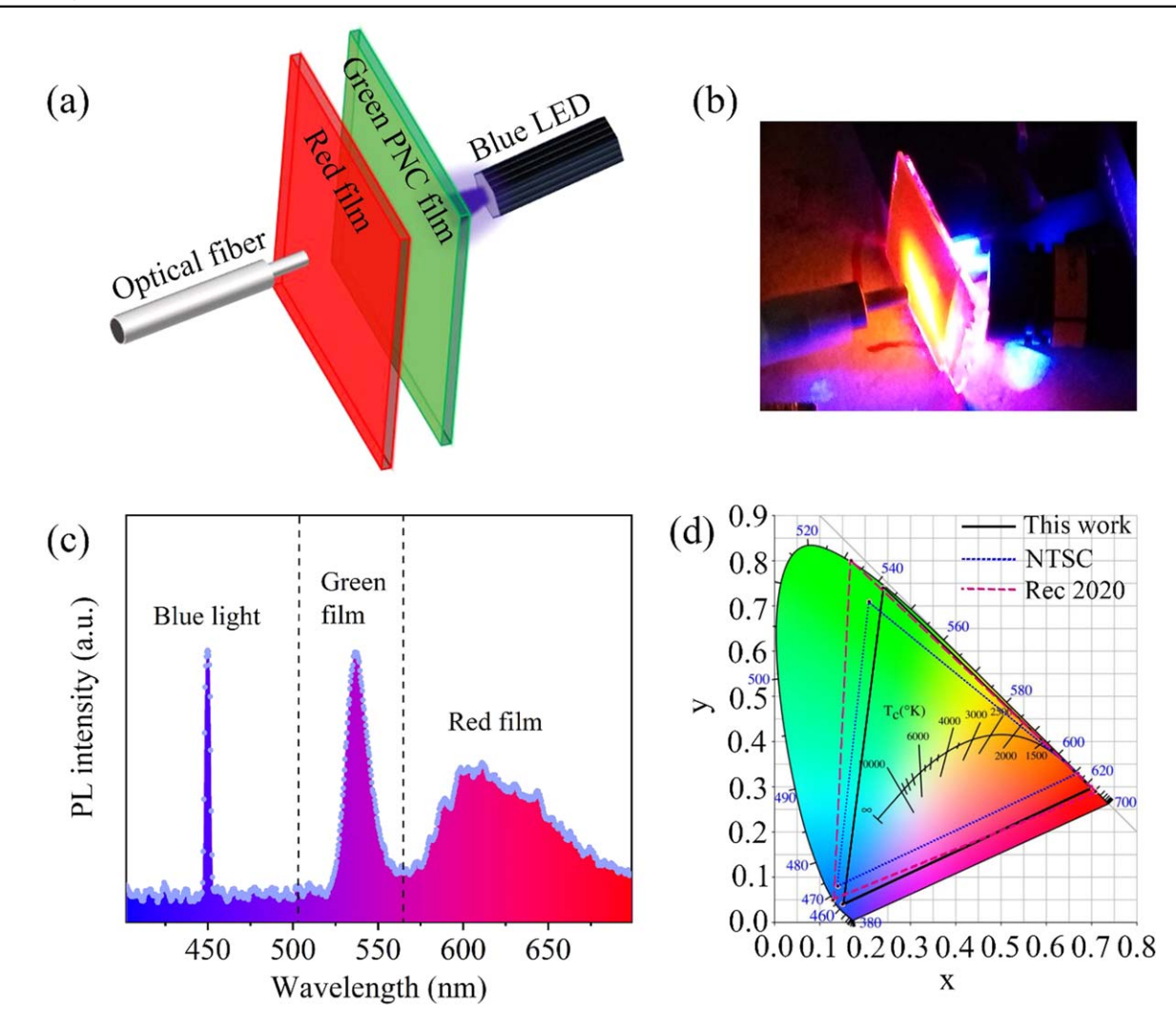


Figure 7. (a) Schematic of the experimental configuration of a backlight with a red-emissive film, a green-emissive PMMA-MAPbBr₃ NC film and a blue light source, (b) optical image of the backlight structure, (c) PL spectrum of backlight, and (d) the color gamut coverage of the PMMA-MAPbBr₃ NC films (black solid line), NTSC 1953 (blue dotted line) and Rec 2020 standard (red dashed line).

optical image of the 'backlight', which emitted strong white light. Figure 7(c) presents the emission spectrum of the 'backlight'. There are three emission peaks of 630 nm (red), 537 nm (green), and 450 nm (blue). Note that stacking the red-emissive film with the green-emissive film leads to a red shift for the PL peak of the red-emissive film under the blue light. Such a trend is consistent with the result reported by Li *et al* [25].

Using the Commission Internationale de l'Eclairage (CIE) color coordinates (table S5, supporting information), we calculated the color gamut of the 'backlight' and found that it covered $\sim 114\%$ and $\sim 85\%$ of that of NTSC 1953 and Rec 2020, respectively (figure 7(d)). Such a result demonstrates that the PMMA-MAPbBr₃ NC films have the potential to be used as an important component for LCD backlight display.

The light efficiency of the backlight is assessed with the PLQY of the PMMA-MAPbBr₃ NC films. The PLQY of the films is 13.12%, which is much lower than the corresponding MAPbBr₃ NCs due to the reabsorption loss in the

PMMA-MAPbBr₃ NC films, as revealed by the small Stokes shift between the PL and absorbance peaks [69].

Conclusion

In summary, we have prepared micro-sized MAPbBr₃ crystals (powders) solely using DI water as solvent for the precursor solution for the first time without conventional, environmental-harmful orgonic solvents, such as DMF and DMSO, and heating at 40 °C. The as-prepared MAPbBr₃ powders were further ultrasonicated in toluene to produce MAPbBr₃ NCs with oleic acid (OA) and oleylamine (OAm) as ligands to stabilize MAPbBr₃ NCs. There are two important chemical reactions contributing to the production of micro-sized MAPbBr₃ crystals—the formation of MA₄PbBr₆ white precipitates from the reaction between MABr and PbBr₂ in the DI water and the formation of MAPbBr₃ powders from the reaction between MA₄PbBr₆ and PbBr₂ at 40 °C. Both the MAPbBr₃ powders and NCs are cubic phase.

The compression with the compressive stress less than and equal to 1.6 MPa has no effect on the PL spectral shape and bandgap of both the PMMA-MAPbBr₃ NC films and the PMMA-CsPbBr₃ NC films. Increasing the compressive stress to 1.6 MPa caused a $\sim 9.5\%$ decrease of the PL peak intensity for the PMMA-MAPbBr₃ NC films and a $\sim 56.8\%$ increase in the PL intensity for the PMMA-CsPbBr₃ NC films. The PMMA-MAPbBr₃ NC films exhibited much better stability in the PL peak intensity than the PMMA-CsPbBr₃ NC films under compression for the compressive stress less than and equal to 1.6 MPa.

Using a PMMA-MAPbBr₃ NC film, a red emissive film and a blue LED (450 nm), we constructed an LCD 'backlight'. The 'backlight' emitted strong white light with red emission (630 nm), green emission (537 nm) and blue emission (450 nm), and the color gamut covered \sim 114% and \sim 85% of that of NTSC 1953 and Rec 2020, respectively.

The method developed in this work provides a simple technique to greenly produce MAPbBr₃ NCs and circumvents the use of harmful organic solvents in the precursor solution. It also opens a new route to produce lead halide perovskite microcrystals and nanocrystals in a large scale, which can benefit for the eco-friendly manufacturing of compression-resistant backlight films for flexible LCD applications.

Experimental section

Materials

The materials used were MABr (99.9%, Sigma-Aldrich), CsBr (99.9%, Beantown Chemical), N,N-dimethylformamide (DMF) (VWR), PbBr₂ (>98%, Strem Chemicals Inc.), oleylamine (OAm) (>50%, TCI America), oleic acid (OA) (Ward's Science), toluene (VWR) and PMMA (99.9%, Sigma-Aldrich). No further purification was performed for all the received chemicals used in this work.

Preparation of MAPbBr₃ powders

MAPbBr₃ powders were prepared with DI water as sole solvent, similar with our previous work [33]. Equimolar (1 mmol) MABr and PbBr₂ were dissolved in 2 ml DI water, and white precipitates were formed in DI water after shaking. The as-obtained white precipitates were placed on a glass plate. The glass plate with the white precipitates was then heated on a hot plate at 40 $^{\circ}$ C for 30 min, leading to the formation of orange MAPbBr₃ powders.

Preparation of MAPbBr3 NCs

The MAPbBr₃ NCs were derived from the orange MAPbBr₃ powders via ultrasonication in toluene, as shown schematically in figure 1. Briefly, 0.02 g of MAPbBr₃ powders were added into 5 ml toluene with 50 μ l OA and 25 μ l OAm to form a suspension. The suspension was ultrasonicated in a water bath for 400 min, and a MAPbBr₃ NC solution was obtained. The final MAPbBr₃ NC solution was produced by a

filtration of the supernatant of ultrasonicated MAPbBr₃ NC solution with a $0.2~\mu m$ syringe filter.

Preparation of CsPbBr3 NCs via an antisolvent method

Using an antisolvent method [23], we prepared CsPbBr₃ NCs. Briefly, a suspension made from DMF (10 ml), OAm (0.5 ml), OA (1 ml), CsBr (0.4 mmol) powder and PbBr₂ (0.4 mmol) powder was prepared. Vigorously stirring the suspension at 30 $^{\circ}$ C overnight led to the formation of a precursor solution. 1 ml of the prepared precursor solution was rapidly dropped in toluene (10 ml) under stirring to form CsPbBr₃ NCs.

Preparation of PMMA-MAPbBr₃ NC films and PMMA-CsPbBr₃ NC films

Moderate MAPbBr₃ NCs were added into a PMMA solution $(0.02 \text{ mg ml}^{-1}, \text{ toluene as solvent})$ to form a PMMA-NC solution with a concentration of 660 mg ml⁻¹. A PET plate $(2.5 \times 2.5 \text{ cm}^2)$ with a layer of the as-obtained PMMA-NC solution coated on its surface was heated on a hot plate at 60 °C for 10 min, leading to the production of a PMMA-MAPbBr₃ NC film. Following the same process with CsPbBr₃ NCs, we obtained a PMMA-CsPbBr₃ NC film.

Fabrication and measurement of PMMA-MAPbBr₃ NC 'backlight' films

A red emissive film was first prepared by spin-coating $100~\mu l$ red ink, which was extracted from a red EXPO marker pen, on a glass plate ($2.5 \times 2.5~cm^2$) at 2500 rpm for 45 s. A green emissive PMMA-MAPbBr₃ NC film and the red emissive film were then vertically combined with a 450 nm blue light-emitting diode (LED) of 100~mW in power (Model:0510, Laserland) to form a white emissive 'LED'. An optical probe was placed perpendicularly to the 'backlight film' to collect light emission.

PL measurements under compression

A compressive force in a range of 0–1000 N was applied onto the films. The force was increased by 100 N every 5 min with a holding time of 2 min at each force. The holding time for the force of 1000 N was 6 min. The PL measurement was conducted after 1 min in the holding stage. The compression was carried out at room temperature on a universal Testing Machine (ESACU200, Shimadzu, Japan). A reflective RO probe was used to record the PL signal (figure 5).

Characterization

TEM (transmission electron microscopy) and HRTEM (high resolution transmission electron microscopy) (Thermo-scientific Talos F200X TEM operated at an accelerating voltage of 200 kV) analyses were performed to examine the morphologies and crystal structures of the perovskite NCs. Energy dispersive X-ray (EDX) spectroscope (Thermo-scientific Super-X System with four windowless silicon-drift-detectors

(SDD) installed on a Talos F200X, TEM) was used to analyze the compositions of the NCs. XRD (X-ray diffraction) measurements were conducted on a diffractometer (Bruker-AXS D8 Discover) with a radiation of CuK_{α} ($\lambda = 1.54060 \, \text{Å}$).

The Rigaku D/Max 2000 X-ray diffractometer unit with a Eulerian cradle was used to conduct the measurement and analysis of the (100) and (200) pole figures of the sample. The alpha rotation angle was from 15° to 90°, and alpha step angle was 5° by the Schulz back-reflection method using CuK_{α} radiation.

PL and TCSPC (time correlated single photon counting) measurements

PL spectra and PL decay curves were collected on a Horiba Scientific Fluoromax Plus-C fluorometer. Entrance and exit slit widths were controlled to give 2 nm bandwidths with an PL integration time of $0.1 \, \mathrm{s}$. For the collection of PL-decay curves, a DeltaHubTM high throughput TCSPC controller and a NanoLED-390 pulsed excitation source (excitation wavelength $393 \pm 10 \, \mathrm{nm}$) were used for TCSPC. PL-decay curves were collected at 425 and 465 nm emission with 5 nm bandpass at a repetition rate of 1 MHz over a measurement time of 200 ns. Instrument response function (IRF) was determined by measuring the scattering of the excitation source with a ludox sample. The fitting of decay curves was obtained using a Horiba Scientific decay analysis software (DAS6).

UV-vis absorption spectrum

UV-vis absorbance was measured using a Thermo Scientific Evolution 201 UV-visible spectrophotometer. The absorbance of samples was measured in transmittance mode (without any correction to the scattering from nanocrystals) in the wavelength range of 300–800 nm with a spectral bandwidth of 1 nm and integration time of 0.1 s.

PLQY (absolute photoluminescence quantum yield) measurements

Absolute PLQYs of samples were determined on a Horiba Scientific Fluoromax Plus-C fluorometer. A solid sample was mounted on a sample stage and placed in an integrating sphere. An excitation wavelength of 390 nm was used for PLQY measurements with a 0.5 nm slit width and 0.1 s integration time. PLQY calculations were done using a Horiba Scientific FluorEssenceTM software. Absolute photoluminescence quantum yield measurements were carried out on a Horiba Scientific fluorescence spectrometer (Fluoromax Plus-C) with an integrating sphere. The Raleigh scattering peak of the excitation and the PL from the specimen were acquired by scanning the emission in a range of 360-650 nm. A blank substrate without specimen was scanned in the same scanning range. The PLQY was calculated using the Horiba Scientific Fluor Essence TM software with a factory acquired integrating sphere correction as PLQY = ((PB - PA)/(LA))- LB)) 100%. Here, (PB - PA) is the number of emitted photons, (LA - LB) is the number of absorbed photons, LA

is total number of incident photons, LB is total photons not absorbed by the specimen, PA is the 'Dark signal' in the emission-wavelength area, and PB is total number of the photons emitted in the emission-wavelength area.

Acknowledgments

FY is grateful for the support by the NSF through the grant CMMI-1854554, monitored by Drs Khershed Cooper and Thomas Francis Kuech, and CBET- 2018411 monitored by Dr Nora F Savage.

Data availability statement

The data that support the findings of this study are available upon reasonable request from the authors.

Conflicts of interest

The authors declare no conflict of interest.

ORCID iDs

Xiaobing Tang https://orcid.org/0000-0003-1416-5212

References

- [1] Chen H-W, Lee J-H, Lin B-Y, Chen S and Wu S-T 2018 Light: Sci. Appl. 7 17168–17168
- [2] Huang Y, Tan G, Gou F, Li M C, Lee S L and Wu S T 2019 J. Soc. Inf. Disp. 27 387–401
- [3] Liu Q and Abbatt J P 2021 Proc. Natl Acad. Sci. 118 e2105067118
- [4] Ko Y-H, Prabhakaran P, Choi S, Kim G-J, Lee C and Lee K-S 2020 Sci. Rep. 10 1–8
- [5] Huang B-L, Guo T-L, Xu S, Ye Y, Chen E-G and Lin Z-X 2019 IEEE Photonics J. 11 1–9
- [6] Lin J, Lu Y, Li X, Huang F, Yang C, Liu M, Jiang N and Chen D 2021 ACS Energy Lett. 6 519–28
- [7] Chen Z, Zhao J, Zeng R, Liu X, Zou B and Xiang W 2021 Chem. Eng. J. 433 133195
- [8] Shu Y, Lin X, Qin H, Hu Z, Jin Y and Peng X 2020 Angew. Chem. 132 22496–507
- [9] Wei Y, Cheng Z and Lin J 2019 Chem. Soc. Rev. 48 310-50
- [10] Wang Y, Li X, Song J, Xiao L, Zeng H and Sun H 2015 Adv. Mater. 27 7101–8
- [11] Kulbak M, Gupta S, Kedem N, Levine I, Bendikov T, Hodes G and Cahen D 2016 J. Phys. Chem. Lett. 7 167–72
- [12] He Y, Matei L, Jung H J, McCall K M, Chen M, Stoumpos C C, Liu Z, Peters J A, Chung D Y and Wessels B W 2018 Nat. Commun. 9 1–8
- [13] Dirin D N, Cherniukh I, Yakunin S, Shynkarenko Y and Kovalenko M V 2016 Chem. Mater. 28 8470–4
- [14] Zhang L, Wang L, Wang K and Zou B 2018 J. Phys. Chem. C 122 15220-5
- [15] Zhao Y-Q, Ma Q-R, Liu B, Yu Z-L and Cai M-Q 2018 Phys. Chem. Chem. Phys. 20 14718–24

- [16] Nagaoka Y, Hills-Kimball K, Tan R, Li R, Wang Z and Chen O 2017 Adv. Mater. 29 1606666
- [17] Xiao G, Cao Y, Qi G, Wang L, Liu C, Ma Z, Yang X, Sui Y, Zheng W and Zou B 2017 J. Am. Chem. Soc. 139 10087–94
- [18] Beimborn J C, Walther L R, Wilson K D and Weber J M 2020 J. Phys. Chem. Lett. 11 1975–80
- [19] Tan Z-K, Moghaddam R S, Lai M L, Docampo P, Higler R, Deschler F, Price M, Sadhanala A, Pazos L M and Credgington D 2014 Nat. Nanotechnol. 9 687–92
- [20] Saparov B and Mitzi D B 2016 Chem. Rev. 116 4558-96
- [21] Kim Y H, Cho H, Heo J H, Kim T S, Myoung N, Lee C L, Im S H and Lee T W 2015 Adv. Mater. 27 1248–54
- [22] Protesescu L, Yakunin S, Bodnarchuk M I, Krieg F, Caputo R, Hendon C H, Yang R X, Walsh A and Kovalenko M V 2015 Nano Lett. 15 3692–6
- [23] Li X, Wu Y, Zhang S, Cai B, Gu Y, Song J and Zeng H 2016 Adv. Funct. Mater. 26 2435–45
- [24] Zhang F, Zhong H, Chen C, Wu X-G, Hu X, Huang H, Han J, Zou B and Dong Y 2015 ACS Nano 9 4533–42
- [25] Li F, Huang S, Liu X, Bai Z, Wang Z, Xie H, Bai X and Zhong H 2021 Adv. Funct. Mater. 31 2008211
- [26] Levchuk I, Osvet A, Tang X, Brandl M, Perea J D, Hoegl F, Matt G J, Hock R, Batentschuk M and Brabec C J 2017 Nano Lett. 17 2765–70
- [27] Park S Y, Park J-S, Kim B J, Lee H, Walsh A, Zhu K, Kim D H and Jung H S 2020 Nat. Sustain. 3 1044–51
- [28] Sadhukhan P, Kundu S, Roy A, Ray A, Maji P, Dutta H, Pradhan S and Das S 2018 Cryst. Growth Des. 18 3428–32
- [29] Chen M, Zhang X, Luo C, Qi R, Peng H and Lin H 2021 ACS Appl. Mater. Interfaces 13 20622–32
- [30] Lin H, Zhang X, Cai L, Lao J, Qi R, Luo C, Chen S, Peng H, Huang R and Duan C 2020 J. Mater. Chem. C 8 5594–9
- [31] Corp S-A 2009 Material Safety Data Sheet for 2-Methylimidazole (Product Number: M50850) (https://sigmaaldrich.com/)
- [32] Program N T 2004 Toxicology and Carcinogenesis Studies of 2-Methylimidazole (CASRN 693-98-1) in F344/N Rats and B6C3F1 Mice (Feed Studies) TR 516 National Toxicology Program Technical Report Series, 1–292
- [33] Tang X, Kothalawala N L, Zhang Y, Qian D, Kim D Y and Yang F 2021 Chem. Eng. J. 425 131456
- [34] Wang H, Wang X, Chen R, Zhang H, Wang X, Wang J, Zhang J, Mu L, Wu K and Fan F 2018 ACS Energy Lett. 4 40-7
- [35] Schmidt L C, Pertegás A, González-Carrero S, Malinkiewicz O, Agouram S, Minguez Espallargas G, Bolink H J, Galian R E and Pérez-Prieto J 2014 J. Am. Chem. Soc. 136 850–3
- [36] Giorgi G, Yoshihara T and Yamashita K 2016 Phys. Chem. Chem. Phys. 18 27124–32
- [37] Akkerman Q A, Park S, Radicchi E, Nunzi F, Mosconi E, De Angelis F, Brescia R, Rastogi P, Prato M and Manna L 2017 Nano Lett. 17 1924–30
- [38] Yu F 2021 Part. Sci. Technol. 39 91-100
- [39] Zhang Y, Wu G, Liu F, Ding C, Zou Z and Shen Q 2020 *Chem. Soc. Rev.* **49** 49–84
- [40] Meinardi F, Colombo A, Velizhanin K A, Simonutti R, Lorenzon M, Beverina L, Viswanatha R, Klimov V I and Brovelli S 2014 Nat. Photon. 8 392–9
- [41] Gurioli M, Martinez-Pastor J, Vinattieri A and Colocci M 1994 Solid State Commun. 91 931–5
- [42] Chouhan L, Ghimire S, Subrahmanyam C, Miyasaka T and Biju V 2020 Chem. Soc. Rev. 49 2869–85
- [43] Tang X, Chen W, Wu D, Gao A, Li G, Sun J, Yi K, Wang Z, Pang G and Yang H 2020 Adv. Sci. 7 1902767

- [44] Chen J, Liu D, Al-Marri M J, Nuuttila L, Lehtivuori H and Zheng K 2016 Sci. China Mater. 59 719–27
- [45] Calado P, Telford A M, Bryant D, Li X, Nelson J, O'Regan B C and Barnes P R 2016 Nat. Commun. 7 1–10
- [46] Huang J, Lei T, Siron M, Zhang Y, Yu S, Seeler F, Dehestani A, Quan L N, Schierle-Arndt K and Yang P 2020 Nano Lett. 20 3734–9
- [47] Yoon Y J, Shin Y S, Park C B, Son J G, Kim J W, Kim H S, Lee W, Heo J, Kim G-H and Kim J Y 2020 Nanoscale 12 21695–702
- [48] Shi D, Adinolfi V, Comin R, Yuan M, Alarousu E, Buin A, Chen Y, Hoogland S, Rothenberger A and Katsiev K 2015 Science 347 519–22
- [49] Yacobi B G and Holt D B 2013 Cathodoluminescence Microscopy of Inorganic Solids (New York: Springer Science & Business Media) (https://doi.org/10.1007/978-1-4757-9595-0)
- [50] Kautsky H 1939 Trans. Faraday Soc. 35 216-9
- [51] Christians J A, Miranda Herrera P A and Kamat P V 2015 J. Am. Chem. Soc. 137 1530–8
- [52] Chuang S L 2012 *Physics of Photonic Devices* (New York: Wiley)
- [53] Zhou J, Wen S, Liao J, Clarke C, Tawfik S A, Ren W, Mi C, Wang F and Jin D 2018 Nat. Photon. 12 154–8
- [54] Lubyshev D, González-Borrero P, Marega E Jr, Petitprez E, La Scala N Jr and Basmaji P 1996 Appl. Phys. Lett. 68 205-7
- [55] Yang F 2021 Phys. Lett. A 401 127346
- [56] Cardona M 2005 Solid State Commun. 133 3-18
- [57] Rubino A, Francisco-López A N, Barker A J, Petrozza A, Calvo M E, Goñi A R and Míguez H 2020 J. Phys. Chem. Lett. 12 569–75
- [58] Keshavarz M, Ottesen M, Wiedmann S, Wharmby M, Küchler R, Yuan H, Debroye E, Steele J A, Martens J and Hussey N E 2019 Adv. Mater. 31 1900521
- [59] Yang H, Li R, Zhang Y, Yu M, Wang Z, Liu X, You W, Tu D, Sun Z and Zhang R 2021 J. Am. Chem. Soc. 143 2601-7
- [60] Savenije T J, Ponseca C S Jr, Kunneman L, Abdellah M, Zheng K, Tian Y, Zhu Q, Canton S E, Scheblykin I G and Pullerits T 2014 J. Phys. Chem. Lett. 5 2189–94
- [61] Wu K, Bera A, Ma C, Du Y, Yang Y, Li L and Wu T 2014 Phys. Chem. Chem. Phys. 16 22476–81
- [62] Zheng K, Zhu Q, Abdellah M, Messing M E, Zhang W, Generalov A, Niu Y, Ribaud L, Canton S E and Pullerits T 2015 J. Phys. Chem. Lett. 6 2969–75
- [63] Tangi M, Mishra P, Janjua B, Prabaswara A, Zhao C, Priante D, Min J-W, Ng T K and Ooi B S 2018 J. Appl. Phys. 123 105702
- [64] Bimberg D, Sondergeld M and Grobe E 1971 Phys. Rev. B 4 3451
- [65] Grandal J, Pereiro J, Bengoechea-Encabo A, Fernandez-Garrido S, Sanchez-Garcia M A, Munoz E, Calleja E, Luna E and Trampert A 2011 Appl. Phys. Lett. 98 061901
- [66] McKittrick J and Shea-Rohwer L E 2014 J. Am. Ceram. Soc. 97 1327–52
- [67] Okamoto K, Funato M, Kawakami Y and Tamada K 2017 J. Photochem. Photobiol. C 32 58–77
- [68] Zhao Y, Li N, Xu C, Li Y, Zhu H, Zhu P, Wang X and Yang W 2017 Adv. Mater. 29 1701513
- [69] Zhou G, Xu Y and Xia Z 2020 ACS Appl. Mater. Interfaces 12 27386–93